Porosity Distributions in a Fluidized Bed with an Immersed Obstacle

Erosion in bubbling fluidized-bed combustors is a serious issue that may affect their reliability and economics. Available evidence suggests that the key to understanding this erosion is detailed knowledge of the coupled and complex phenomena of solids circulation and bubble motion. A thin transparent "two-dimensional" rectangular fluidized bed with an obstacle served as a rough model for a fluidized-bed combustor. This model was studied experimentally and computationally using two hydrodynamic equation sets. The computed hydrodynamic results agree reasonably well with experimental data. Bubble frequencies and sizes compare well with those obtained from analyzing a high-speed motion picture frame-by-frame. Time-averaged porosities computed from both models agree with time-averaged porosity distributions measured with a gamma-ray densitometer. The principal differences between the data and the computations in this paper are due to asymmetries present in the experiment and to the simplified solids rheology used in the hydrodynamic models.

J. X. Bouillard
R. W. Lyczkowski
Argonne National Laboratory
Energy and Environmental
Systems Division
Argonne, IL 60439

D. Gidaspow
Illinois Institute of Technology
Department of Chemical Engineering
Chicago, IL 60616

Introduction

Bubbling fluidized-bed combustors are being built as a means of burning high-sulfur coals in an environmentally acceptable manner. Although this technology has reached a commercial status, understanding of solids motion and its effects on erosion of the heat-exchanger tubes immersed in fluidized beds remains inadequate [NCB (IEA Grimethorpe) Ltd., 1985]. To understand the mechanics of solids motion in fluidized beds with heat exchangers, fluidized beds with immersed obstacles have been studied experimentally by a number of authors (Buyevich et al., 1986; Fakhimi and Harrison, 1980; Glass and Harrison, 1964; Levy et al., 1986; Loew et al., 1979; Mao and Potter, 1986; Rowe and Everett, 1972; Rowe and Masson, 1981; Xavier et al., 1978).

Solids motion has been simulated with supercomputers, as reviewed by Gidaspow (1986), using hydrodynamic models originally developed by Jackson (1963), with significant contributions, for example, by Fanucci et al. (1979), Garg and Pritchett (1975), Pritchett et al. (1978), and Soo (1967). Many of these models, however, still lack experimental validation, so they cannot presently be considered reliable as future design tools.

The major purpose of this study is to experimentally validate two hydrodynamic models found in the literature for the transient behavior of a two-dimensional fluidized bed with an immersed obstacle. These two models are:

1) The annular flow model with pressure drops in both the gas and solids phases (Hydrodynamic Model A) (Nakamura and Capes, 1973)

2) The model with the entire pressure drop in the fluid phase only, first proposed by Rudinger and Chang (1964) and extended by Lyczkowski (1978) (Hydrodynamic Model B).

Predicted instantaneous and time-averaged porosities are compared with experimentally measured values.

Experimental Apparatus

A thin "two-dimensional" rectangular transparent plastic fluidized bed having a rectangular slit jet and an immersed obstacle was constructed (see Figure 1). In this bed, a two-dimensional slice of a fluidized-bed combustor was simulated. The rectangular jet represented a coal feed port and the obstacle represented a horizontal heat-exchanger tube within the bed. This transparent two-dimensional bed permitted visual observation of bubbles and solids motion. The bed cross section was 40-cm-wide and 3.81-cm-deep, and the jet nozzle was a 1.27-cm by 3.81-cm rectangular slit. A rectangular plexiglass obstacle, 9.74 cm high by 2.54 cm wide, was placed at 9.74 cm above the jet. Both the distributor plates and the jet nozzle were covered with 80-mesh stainless steel wire mesh. The distributor was made of a packed bed of 3-mm-dia. polyester particles. In order to achieve uniform fluidization, the distributor section was designed in

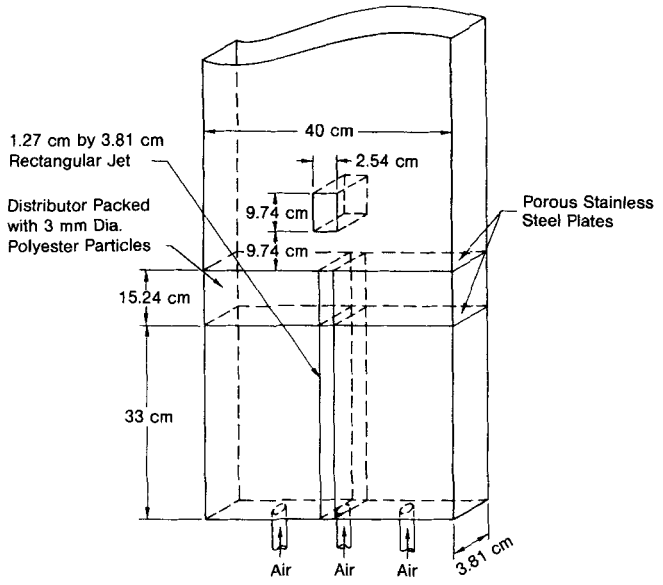

Figure 1. Two-dimensional cold fluidized bed with a rectangular central jet and a rectangular obstacle.

such a way that the pressure drop through the distributor section was approximately 20% of the total pressure drop (Kunii and Levenspiel, 1969).

Air was supplied by three separate systems with individual controls and flowmeters: two for the air plenum supplying air to fluidize the bed particles and one for the air jet. The top of the bed was exposed to the atmosphere. In a typical run, solids were first loaded into the rectangular column to give a static bed height of 28 cm. The bed was then fluidized to satisfy the conditions summarized in Table 1. The minimum-fluidization velocity was obtained by finding the intersection between pressure drop vs. flow rate curves in the fixed-bed and in the fluidized-bed regions (Seo, 1985).

Experimental Results

At minimum-fluidization conditions, we observed bubbling on the vertical sides of the obstacle by analyzing a high-speed motion picture frame-by-frame. This phenomenon has been previously reported in the literature (Buyevich et al., 1986; Glass and Harrison, 1964; Grace, 1982; Loew et al., 1979). Buyevich et al. (1986), who studied a rectangular obstacle in two-dimensional fixed and fluidized beds, explained the phenomenon of bubble formation as arising from the low gas-flow resistance next to the obstacle (due to high local porosity). The resultant excess gas flow, which was measured in a fixed bed to be 5–10 times that in the bulk of the bed, produced the bubbles.

Table 1. Fluidized-Bed Operating Conditions*

Parameter	Value
Particle Mean Dia. (μm)	503
Particle Density (g/cm^3)	2.44
Particle Sphericity	1.00
Min. Fluidiz. Porosity	0.42
Min. Fluidiz. Velocity (cm/s)	26
Temperature (°C)	22
Min. Fluidiz. Bed Height (cm)	29.2
Pres. at Top of Bed (kPa)	101.3
Jet Flow Rate (m/s)	5.78

*Material is glass beads; fluid carrier is air.

We found that bubbles often formed in alternation at the surface of the obstacle—one at one side, then another at the opposite side. Once formed, these bubbles did not move up along the center of the bed; instead, they moved preferentially away from the defluidized region located just above the obstacle.

Bubbles formed in the presence of a central 578-cm/s jet and a centrally located obstacle, as shown in Figure 1, were compared with those obtained under the same experimental conditions in a bed without an obstacle (Gidaspow, 1985; Seo, 1985). High-speed motion pictures were analyzed frame-by-frame to quantitatively determine the formation, shape and velocity of bubbles. This technique has been routinely applied to high speed motion pictures and videos to analyze bubble and solids motion in fluidized beds, e.g., by Levy et al. (1986), Pemberton and Davidson (1986), Levy et al. (1983), and Glass and Harrison (1964). These motion pictures of 2.5-s duration were shot with a 16-mm high-speed Fastax movie camera (800 frames per second). The camera was electronically connected to the solenoid valve of the jet so that movie and jet were started simultaneously. In Figure 2, a sequence of three frames from the actual high-speed movie was reproduced illustrating the bubble evolution. Shown are the initial bubble formation (0.105 s), propagation (0.236 s), and bursting through the bed at 0.315 s. From frames such as these, it was possible to compare quantitatively the experimental bubble sizes formed with and without the obstacle. Table 2 shows that with the obstacle centrally located, the shape of experimental bubbles was no longer cylindrical, but tended to be elongated.

Repeated frame-by-frame analysis of the high-speed movie indicated that the solids flowed up in the jet region, were deflected away from the obstacle, slid down along the walls and along the slumped region edges, and moved back into the jet region. Because of this solids motion, they were continuously reinjected at the jet mouth, and the jet nozzle was found to be periodically blocked by the solids at a characteristic frequency of approximately 9–10 Hz.

Seo (1985) measured porosity fluctuations in an identical bed not containing a central obstacle and used a densitometer consisting of a sodium iodide (NaI) scintillation counter to detect gamma rays from a C_s-137 source. These gamma-ray measurements were then converted into porosities. Seo's bed dimensions and gas/solids system were identical to those presented in Figure 1 and Table 1. Seo's results in Figure 3 show the inherent periodic behavior of a fluidized bed. Each oscillation corresponds to the passage of a bubble at a specific location in the bed. The bubbling frequency of approximately 3–4 Hz (defined to be the number of peaks per second above a porosity $\epsilon \geq 0.8$) indicated in Figure 3 is somewhat lower than the bubbling frequency of approximately 4–5 Hz around the obstacle obtained in this study by repeated frame-by-frame analysis of the high-speed motion pictures. This technique constitutes a viable alternative to measuring fluctuating porosities with a densitometer (not done in our study). The frequency of the bubble formation at the jet mouth was determined to be about 9–10 Hz.

In our study, time-averaged porosities were obtained using a C_s-137 gamma-ray source and detected with an ionization gauge. Earlier exploratory time-averaged porosity measurements indicated axial symmetry about the bed centerline (Gi-

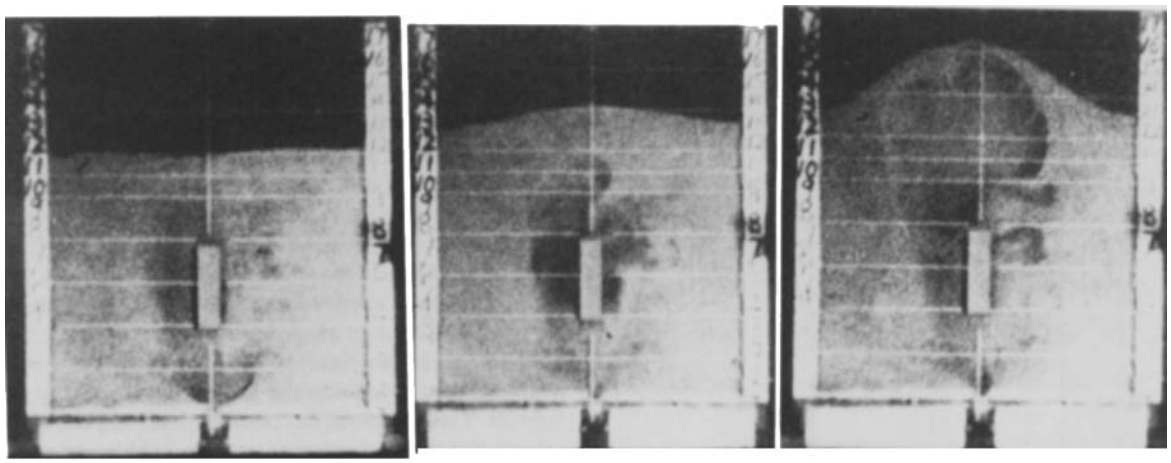

a b c

a. Bubble formation at the distributor, 0.105 s
b. Bubble propagation around the obstacle, 0.236 s
c. Bubble bursting at the top of the bed, 0.315 s

Figure 2. Evolution of an experimental bubble in a two-dimensional rectangular fluidized bed with a central jet and an immersed obstacle.

daspow et al., 1983a). Therefore, in this study, measurements were obtained for only half the bed at various positions from the bed centerline and heights above the distributor, amounting to 271 spatial locations (Bouillard, 1986). Details of the calibration of this apparatus are explained by Bouillard (1986), Seo (1985), and Gidaspow et al. (1983a). Porosities were time-averaged over a period of 100 s, which was well above the natural period of the fluidized bed.

These two-dimensional time-averaged porosity contours were reflected about the bed centerline and are shown in Figure 4. Curves of constant porosity (isoporosity contours) emanate from the central jet and reach the top of the bed, where they curve horizontally toward the walls. A somewhat defluidized region is found just above the obstacle. Other isoporosity contours (porosity, ϵ, equal to 0.60, 0.50 and 0.45) are almost straight lines that originate from the central jet and reach the top of the bed.

As expected, the jet region was dilute, and the solids were pushed by the gas jet to the walls of the bed to create a slumped region of high solids concentration ($\epsilon = 0.4$) in the lower part of the bed near the distributor. A dilute region ($\epsilon = 0.8$–0.95) is found near the initial minimum fluidization bed height of 29.2 cm. This region represents the splash zone, where bubbles burst at the bed interface.

Table 2. Computed and Experimental Bubble Sizes in a Two-Dimensional Fluidized Bed

Experimental Conditions	Bubble Size	
	Height (cm)	Width (cm)
With Obstacle (0.236 s)		
Experimental	22	15
Simulated	22	18
Without Obstacle*		
(Exp. only)	14	12

*From Seo (1985)

Hydrodynamic Models and Constitutive Relations

Hydrodynamic models of fluidization use the principles of conservation of mass, momentum, and energy. In this section, the separate phase continuity equations and the momentum equations for two-dimensional, transient, isothermal two-phase flow (in Cartesian coordinates), which form the basis of the FLUFIX code, are given for two hydrodynamic models.

Hydrodynamic Model A

The set of momentum equations presented below is sometimes referred to as the annular flow model (Nakamura and Capes, 1973) or the basic equation set (Lee and Lyczkowski, 1981). In this study, we refer to this set as "Hydrodynamic Model A."

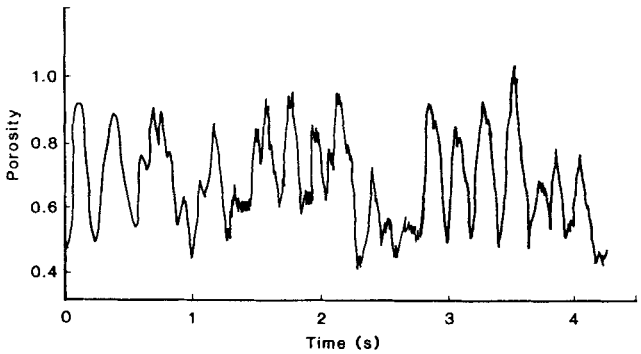

Figure 3. Typical porosity oscillations in a two-dimensional fluidized bed with a central jet and no obstacle, 3.81 cm above the Jet Mouth.

Porosity was measured with a gamma-ray technique. Source: Seo (1985).

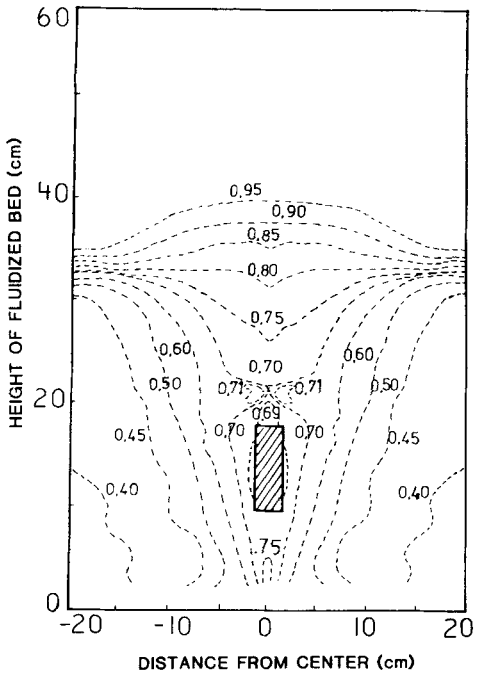

Figure 4. Experimental time-averaged porosity distribution obtained from a two-dimensional fluidized bed with a rectangular jet and an immersed obstacle.

Absolute Porosity Measurement Error = ±2%

Gas-Phase Continuity

$$\frac{\partial}{\partial t}(\rho_g\epsilon) + \frac{\partial}{\partial x}(\epsilon\rho_g U_g) + \frac{\partial}{\partial y}(\epsilon\rho_g V_g) = 0 \tag{1}$$

Solids-Phase Continuity

$$\frac{\partial}{\partial t}[\rho_s(1-\epsilon)] + \frac{\partial}{\partial x}[\rho_s U_s(1-\epsilon)] + \frac{\partial}{\partial y}[\rho_s V_s(1-\epsilon)] = 0 \tag{2}$$

Gas-Phase Momentum in x-Direction

$$\frac{\partial}{\partial t}(\rho_g\epsilon U_g) + \frac{\partial}{\partial x}(\rho_g\epsilon U_g U_g) + \frac{\partial}{\partial y}(\rho_g\epsilon V_g U_g) = -\epsilon\frac{\partial P}{\partial x} + \beta_{A,x}(U_s - U_g) \tag{3}$$

Solids-Phase Momentum in x-Direction

$$\frac{\partial}{\partial t}[\rho_s(1-\epsilon)U_s] + \frac{\partial}{\partial x}[\rho_s(1-\epsilon)U_s U_s] + \frac{\partial}{\partial y}[\rho_s(1-\epsilon)V_s U_s] = -(1-\epsilon)\frac{\partial P}{\partial x} + \beta_{A,x}(U_g - U_s) + G(\epsilon)\frac{\partial \epsilon}{\partial x} \tag{4}$$

Gas-Phase Momentum in y-Direction

$$\frac{\partial}{\partial t}(\rho_g\epsilon V_g) + \frac{\partial}{\partial x}(\rho_g\epsilon U_g V_g) + \frac{\partial}{\partial y}(\rho_g\epsilon V_g V_g) = -\epsilon\frac{\partial P}{\partial y} + \beta_{A,y}(V_s - V_g) - \rho_g\epsilon g \tag{5}$$

Solids-Phase Momentum in y-Direction

$$\frac{\partial}{\partial t}[\rho_s(1-\epsilon)V_s] + \frac{\partial}{\partial x}[\rho_s(1-\epsilon)U_s V_s] + \frac{\partial}{\partial y}[\rho_s(1-\epsilon)V_s V_s] = -(1-\epsilon)\frac{\partial P}{\partial y} + \beta_{A,y}(V_g - V_s) - \rho_s(1-\epsilon)g + G(\epsilon)\frac{\partial \epsilon}{\partial y} \tag{6}$$

The solids elastic modulus, $G(\epsilon)$, is used to calculate the normal component of the solids Coulombic stress through the following relationship:

$$\partial\tau = \frac{\partial\tau}{\partial\epsilon}\partial\epsilon = G(\epsilon)\partial\epsilon \tag{7}$$

following Garg and Pritchett (1975).

Six nonlinear, coupled, partial differential equations must be solved for the six dependent variables: the void fraction, ϵ; the pressure, P; and the gas velocity components U_g and V_g and the solids velocity components U_s and V_s in the x- and y-directions, respectively. The equations are written in a form similar to that used in the K-FIX computer code, from which FLUFIX has been developed (Rivard and Torrey, 1977). Stresses associated with gas and solids viscosities have been deleted, thus simplifying the solids rheology. Rivard and Torrey found that, for many applications, these terms were unimportant and significantly increased the computational effort (Rivard and Torrey, 1979). The conservation equations in the FLUFIX code are solved in conservation-law form in two-dimensional Cartesian and axisymmetric cylindrical coordinates using the Implicit Multifield (IMF) numerical technique (Harlow and Amsden, 1975). Cartesian coordinates were used in the present computations.

The treatment of the pressure-gradient term in the gas- and solids-phase momentum equations (Eqs. 3–6) in the absence of all viscous stresses and without the solids elastic modulus, $G(\epsilon)$, results in an initial-value problem that is ill-posed, i.e., one possessing complex characteristics, as is discussed in detail by Lyczkowski et al. (1978). However, as shown by Stewart (1979), numerical methods for such systems of equations introduce dissipation and are conditionally stable. Prosperetti (1979) showed that the SIMMER II semiimplicit numerical procedure (which is essentially the K-FIX numerical procedure retained basically unchanged in this paper) used to solve Hydrodynamic Model A is also conditionally stable.

Fanucci et al. (1979) analyzed the characteristics for Hydrodynamic Model A for one-dimensional incompressible flow retaining the solids elastic modulus, $G(\epsilon)$. One characteristic

direction, C, is as follows:

$$C = \left(\frac{\rho_s}{\epsilon_s} + \frac{\rho_g}{\epsilon_g}\right)^{-1/2}\left[\frac{-(V_g - V_s)^2}{\frac{\epsilon_g}{\rho_g} + \frac{\epsilon_s}{\rho_s}} + \frac{G(\epsilon)}{\epsilon_s}\right]^{1/2} \tag{8}$$

Equation 8 suggests that the conditional stability of the K-FIX numerical procedure should increase because as the solids elastic modulus, $G(\epsilon)$, becomes increasingly large, real characteristic directions result. Travis et al. (1976) showed by using a detailed linear stability analysis that the inclusion of two-phase rheological dissipative viscous stresses also conditionally stabilizes Hydrodynamic Model A. Jackson (1985) arrived at similar conclusions.

Hydrodynamic Model B

In view of the conditional stability of Hydrodynamic Model A due to the existence of the complex characteristics, we have adopted another hydrodynamic model. This well-posed model (i.e., one possessing all real characteristics) was given first by Rudinger and Chang (1964) and was extended by Lyczkowski (1978). This second set of momentum equations, which we call "Hydrodynamic Model B," is written as follows (the continuity equations, Eqs. 1 and 2, are common to both models):

Gas-Phase Momentum in x-Direction

$$\frac{\partial}{\partial t}(\rho_g \epsilon U_g) + \frac{\partial}{\partial x}(\rho_g \epsilon U_g U_g) + \frac{\partial}{\partial y}(\rho_g \epsilon V_g U_g) = -\frac{\partial P}{\partial x} + \beta_{B,x}(U_s - U_g) \tag{9}$$

Solids-Phase Momentum in x-Direction

$$\frac{\partial}{\partial t}[\rho_s(1-\epsilon)U_s] + \frac{\partial}{\partial x}[\rho_s(1-\epsilon)U_s U_s] + \frac{\partial}{\partial y}[\rho_s(1-\epsilon)V_s U_s] = \beta_{B,x}(U_g - U_s) + G(\epsilon)\frac{\partial \epsilon}{\partial x} \tag{10}$$

Gas-Phase Momentum in y-Direction

$$\frac{\partial}{\partial t}(\rho_g \epsilon V_g) + \frac{\partial}{\partial x}(\rho_g \epsilon U_g V_g) + \frac{\partial}{\partial y}(\rho_g \epsilon V_g V_g) = -\frac{\partial P}{\partial y} + \beta_{B,y}(V_s - V_g) - \rho_g \epsilon g \tag{11}$$

Solids-Phase Momentum in y-Direction

$$\frac{\partial}{\partial t}[\rho_s(1-\epsilon)V_s] + \frac{\partial}{\partial x}[\rho_s(1-\epsilon)U_s V_s] + \frac{\partial}{\partial y}[\rho_s(1-\epsilon)V_s V_s] = \beta_{B,y}(V_g - V_s) - \rho_s(1-\epsilon)g + G(\epsilon)\frac{\partial \epsilon}{\partial y} \tag{12}$$

Differences between Models

The major difference between Eqs. 3–6 (Hydrodynamic Model A) and Eqs. 9–12 (Hydrodynamic Model B) is that, in the latter, all pressure drops are in the gas-phase momentum equations, with none in the solids-phase momentum equations.

The drag coefficient for Hydrodynamic Model B must be modified to satisfy Archimedes' principle and the usual minimum fluidization relationship as given, for example, by Kunii and Levenspiel (1969). An analysis following Gidaspow (1986) traces the steps required to ensure these necessary conditions.

The y-direction (vertical) momentum equations for Hydrodynamic Model A (Eqs. 5 and 6), with negligible acceleration and Coulombic stress, are as follows:

$$0 = -\epsilon\frac{\partial P}{\partial y} + \beta_{A,y}(V_s - V_g) - \rho_g \epsilon g \tag{13}$$

$$0 = -(1-\epsilon)\frac{\partial P}{\partial y} + \beta_{A,y}(V_g - V_s) - \rho_s(1-\epsilon)g \tag{14}$$

The sum of Eqs. 13 and 14 gives the mixture momentum equation, usually called the manometer formula:

$$-\frac{\partial P}{\partial y} = g[\rho_g \epsilon + \rho_s(1-\epsilon)] \tag{15}$$

Equation 15 states that the total static pressure drop equals the weight of the bed. Solving for $(\partial P)/(\partial y)$ from Eq. 13 and combining with Eq. 15 gives

$$-\left(\frac{\beta_{A,y}}{\epsilon}\right)(V_s - V_g) = (1-\epsilon)(\rho_s - \rho_g)g = -\left.\frac{\Delta P}{\Delta y}\right|_{\text{frict}} \tag{16}$$

Equation 16 found in Kunii and Levenspiel's book (1969) makes it clear that the principal contribution to the total static pressure drop in fluidization given by Eq. 15 is due to the drag. Equation 16 states that the frictional loss equals the buoyant force and is used to compute the fluidizing velocity at minimum fluidization.

The y-direction (vertical) momentum equations for Hydrodynamic Model B (Eqs. 11 and 12), with negligible acceleration and coulombic stress, are as follows:

$$0 = -\frac{\partial P}{\partial y} + \beta_{B,y}(V_s - V_g) - \rho_g \epsilon g \tag{17}$$

$$0 = +\beta_{B,y}(V_g - V_s) - \rho_s(1-\epsilon)g \tag{18}$$

The sum of Eqs. 17 and 18 also gives the mixture momentum equation (manomometer formula), Eq. 15. Solving for $(\partial P)/(\partial y)$ from Eq. 17 and combining with Eq. 15 gives

$$-\beta_{B,y}(V_s - V_g) = (1-\epsilon)\rho_s g \tag{19}$$

By combining Eqs. 16 and 19, the fluid-particle friction coefficients $\beta_{A,y}$ and $\beta_{B,y}$ are related as follows:

$$\beta_{B,y} = \frac{\beta_{A,y}\rho_s}{\epsilon(\rho_s - \rho_g)} \simeq \frac{\beta_{A,y}}{\epsilon} \tag{20}$$

The relationship given by Eq. 20 ensures that Archimedes' principle is not violated and yields the same minimum fluidization relationship for Hydrodynamic Model B as given by Kunii and Levenspiel (1969). This relationship for β_B holds for liquid fluidized beds as well as gas fluidized beds at elevated pressure. The interphase drag expressions in the x-direction are related in the same way, for similar reasons:

$$\beta_{B,x} \simeq \frac{\beta_{A,x}}{\epsilon} \tag{21}$$

Closure Constitutive Relationships

For the dense region, the well known Ergun (1952) equation (Bird et al., 1960; Kunii and Levenspiel, 1969) obtained from packed bed pressure drop data for $(-\Delta P)/\Delta y|_{\text{frict}}$ is used to obtain β_A. In the dilute region, β_A is obtained from the standard drag function for a single sphere (Bird et al., 1960) corrected empirically by Wen and Yu (1968) to account for a small packing effect. The transition between these two expressions is made at a porosity of 0.8. These expressions may be summarized (for the y-direction) as follows:

$$\beta_{A,y} = \begin{cases} 150\dfrac{(1-\epsilon)^2\mu_g}{\epsilon(d_p\phi_s)^2} + 1.75\dfrac{\rho_g|V_g - V_s|(1-\epsilon)}{(d_p\phi_s)} & \epsilon \le 0.8 \quad (22a) \\ \dfrac{3}{4}C_{dy}\dfrac{\epsilon|V_g - V_s|\rho_g(1-\epsilon)}{(d_p\phi_s)}\epsilon^{-2.7} & \epsilon > 0.8 \quad (22b) \end{cases}$$

$$C_{dy} = \begin{cases} 24(1 + 0.15)\,Re_y^{0.687})/Re_y & Re_y \le 1{,}000 \quad (23a) \\ 0.44 & Re_y > 1{,}000 \quad (23b) \end{cases}$$

where the Reynolds number is given by

$$Re_y = \frac{|V_g - V_s|d_p\phi_s\rho_g\epsilon}{\mu_g} \tag{24}$$

Analagous expressions are used for the x-direction.

Equations 22 through 24 have been used to compute fluidization characteristics using Hydrodynamic Model A. Previously computed velocity profiles, bubble shapes and sizes at low and high pressures have agreed with experiments (Gidaspow, 1986), therefore, there was no need to modify β_A for calculations involving obstacles.

In the limit of no solids and gas acceleration, Hydrodynamic Models A and B reduce correctly to the well-known fluidization equations as given in Kunii and Levenspiel (1969). As has been already shown, the sum of the solids and the gas momentum equations gives the mixture momentum equations, which are accepted by almost all two-phase-flow investigators.

To complete the two sets of momentum equations, a normal component of solids-phase stress, τ, (sometimes associated with solids-phase pressure or particle-to-particle interactions), is retained in the solids-phase momentum equations (Eqs. 4, 6, 10 and 12). A general formulation of such a term would include the effects of porosity, pressure, and the displacement tensors of solids velocity, gas velocity, and relative velocity. Such a formulation, with appropriate material constants, is not available today. This solids stress is physically necessary to prevent the particles from compacting to unreasonably high solids volume fractions. The static normal component of this stress, usually called the Coulomb's component, has been used by Concha and Bustos (1987), Ettehadieh and Gidaspow (1984), Gidaspow (1986), Gidaspow et al. (1981, 1982, 1983a,b), Gidaspow and Ettehadieh (1983), Padhye and O'Brien (1984), and Pritchett et al. (1978).

This Coulomb's component is usually taken to be zero at and above minimum fluidization conditions. (See the section on Differences Between Models.) Below minimum fluidization, this Coulombic component becomes increasingly important as the particles contact each other. In fact, it acts as a repulsive pressure at high solids fraction. Molerus interpreted this phenomenon as the direct result of Hertz's contact pressure, which is a function of the particle Young's elasticity modulus (Molerus, 1975). This interpretation allows us to relate solids stress measurements to material properties of the powder.

The measurement of this term has been reported by Rietema and Mutsers (1973) and by Piepers et al. (1984). There is considerable disagreement as to the exact form of this stress. Shinohara summarizes 15 different expressions correlating the solids repulsive pressure with the bulk solids volume fraction (1984). Unfortunately, these relations lack any strong physical basis.

To place the Coulomb's stress component in perspective, we must consider the mechanisms of powder compaction (Shinohara, 1984; Orr, 1966). The motivation for the most generally satisfactory expression is the experimental observation that plotting the logarithm of consolidating pressure vs. particle volume yields a substantially straight line for both metallic and nonmetallic powders undergoing compaction (Orr, 1966). We used Orr's (1966) simple theory to derive a generalized solids elastic modulus coefficient, $G(\epsilon)$, of the form

$$G(\epsilon)/G_o = \exp\,[-c(\epsilon - \epsilon^*)] \tag{25}$$

where c (called the compaction modulus) is the slope of $\ln(G)$ vs. ϵ, and ϵ^* is the compaction gas-phase volume fraction. The normalizing units factor, G_o, has been taken to be 1.0 Pa for convenience. For ϵ greater than ϵ^*, the exponent of Eq. 25 becomes negative so that the solids elasticity modulus G becomes smaller as ϵ becomes larger. However, for ϵ less than ϵ^*, the elasticity modulus G becomes larger as ϵ decreases, thus preventing the solids-phase volume fractions from being much larger than $1 - \epsilon^* = \epsilon_s^*$.

Equation 25 is a convenient and consistent expression with which to interpret the physical significance of solids pressure data. For this purpose, we have converted the following into the

Table 3. Solids Elastic Modulus Parameters

Modulus	c	ϵ^*	Reference
G_1	600	0.376	This Study
G_2	500	0.422	Gidaspow and Syamlal (1985)
G_3	20	0.62	Gidaspow and Ettehadieh (1983) Rietema and Mutsers (1973)

form of Eq. 25: 1) the Rietema and Mutsers data (1973), as curve fit by Gidaspow and Ettehadieh (1983); 2) the expression used by Gidaspow and Syamlal (1985) for solids-gas critical flow; and 3) the expression we have been using for hydrodynamics and erosion calculations for a fluidized bed containing an obstacle. The parameters obtained are given in Table 3, and the respective elastic moduli are plotted in Figure 5.

Theoretically, the Coulombic stress component should be zero at and above minimum fluidization. For Hydrodynamic Model A, we needed a Coulombic stress component to stabilize the numerical solution procedure. For Hydrodynamic Model B, we could have set this term to zero above minimum fluidization. As can be seen in Figure 5, in the dilute region, all values of the solids elastic moduli obtained from our generalized model, Eq. 25, are essentially zero. Almost all the results in this paper are above minimum fluidization and, therefore, precise numerical values of the solids elastic modulus in these computations are not important.

In the above analysis, $G(\epsilon) = 1.0$ Pa when $\epsilon = \epsilon^*$. The Rietema and Mutsers model (1973) is inappropriate to keep the bed from compacting, because the model was developed for data taken at a much higher compaction porosity (0.62), and the compaction modulus is very low. Computed porosities below 0.2 have resulted with this model. Gidaspow and Syamlal's model (1985), developed from solids-gas flow data through aerated hoppers (Altiner and Davidson, 1980), is appropriate at a compaction porosity near minimum fluidization (0.422). The compaction modulus is high because the particles are being compacted as they flow down through the hopper. Our model has a somewhat higher compaction modulus and a lower compaction porosity, more appropriate for a packed bed (0.376). The use of these parameters is necessary because of the greater compaction resulting from solids striking the obstacle.

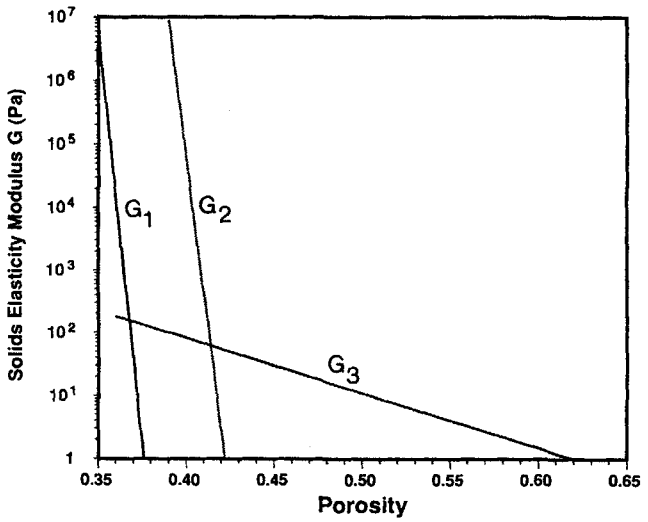

Figure 5. Three solids elastic moduli—G_1, G_2, and G_3—plotted against porosity.

Hydrodynamic Computational Results and Comparisons with Data

The basic model setup is the same as that published by Gidaspow and Ettehadieh, as shown in Figure 6 (Gidaspow and Ettehadieh, 1983). The computational region is 19.685-cm-wide and 58.44-cm-high. The cell dimensions are $\Delta x = 0.635$ cm and $\Delta y = 4.87$ cm, so that the number of computational cells is 31 in the x-direction and 12 in the y-direction, for a total of 372. In Figure 6, the numbers in parentheses refer to key cell numbers (I, J). Symmetry above the central jet is assumed, so the actual bed width is 39.37 cm. In previous modeling work without an obstacle, symmetry was assumed, and the agreement with experimental data was good (Gidaspow, 1986). The jet half-width is 0.635 cm (one cell width). The jet velocity is 578 cm/s, and the secondary air velocity of 26.0 cm/s maintains the bed without a jet at minimum fluidization. The particle diameter is 503 μm, and the density is 2.44 g/cm^3 the same as used in the experiment. The obstacle is placed two nodes above the jet and is two nodes wide by two nodes high (1.27 cm wide by 9.74 cm high). Because the initial bed height is 29.2 cm (six cells high), the obstacle lies completely within the bed. Although this configuration is not typical of fluidized-bed combustor (FBC) geometries, it was selected because: 1) it is similar to the model without the obstacle, so that prior experience is relevant; and 2) it serves to further validate the hydrodynamic model.

The boundary conditions are described here. At the inlet ($J = 2$), the axial gas velocity is set equal to the experimentally

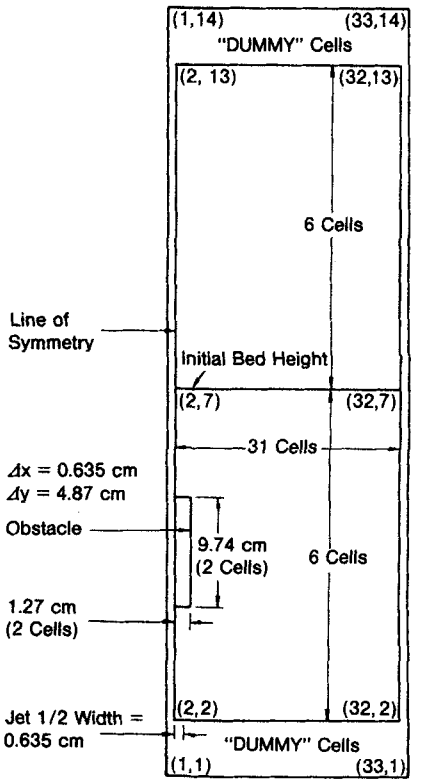

Figure 6. FLUFIX computational mesh for coarse mesh, showing obstacle location.

determined minimum-fluidization superficial velocity of 26.0 cm/s. There are no solids entering, so the inlet porosity is set to 1.0. The pressures in the dummy cells at the top ($J = 14$) are set equal to atmospheric pressure (101.3 kPa), and $V_s = 0$ at the exit ($J = 13$); that is, a wire mesh is simulated to prevent solids carryover. The pressures in the bottom row of dummy cells ($J = 1$) are set equal to atmospheric pressure plus 1.2 times the total bed weight (105.5 kPa) to simulate the distributor plate pressure drop measured in the experiment. On all solid surfaces except the inlet, outlet, and line of symmetry, no-slip boundary conditions are used (i.e., normal and tangential velocities for each phase are set equal to zero).

Initially, the lateral gas velocity is zero, the axial gas velocity is equal to the interstitial gas velocity at minimum fluidization, and the solids lateral and axial velocities are zero. The bed volume fraction at minimum fluidization, ϵ_{mf}, is uniform at 0.42. The initial pressure distribution corresponds to the hydrostatic bed height. At time t greater than zero (0^+), the gas flow through the jet into cell (2, 2) is increased to 578 cm/s. A fixed time step of 0.1 ms was used. Typical running time on an IBM 3033 computer was about one hour for each second of transient time in the simulation. The computations were performed before high-speed (800 frame/s) motion pictures were taken of a flow-visualization experiment modified to include an obstacle. The base-case computations use Hydrodynamic Model A and solids elastic modulus G_1 (Table 3).

Figure 2b reproduces a still frame from this motion picture at about 0.25 s into the transient state (there is an uncertainty of about 0.02 s in the time the jet was turned on), illustrating the formation of the first bubble. The numbers above the white horizontal lines are the bed height in inches. The bed height has increased from its initial value of 29.2 cm (11.5 in.) to 35.6 cm (14 in.) near the bed center and to 33 cm (13 in.) near the bed edge. The top boundary of the bubble is between 25.4 and 30.5 cm (between 10 and 12 in.), and the bubble half width is between 5.1 and 10.2 cm (between 2 and 4 in.) from the bed center.

The left side of Figure 7 shows a dot plot representation of the computed porosity distribution at 0.255 s. The dots are distributed randomly throughout each computational cell. The lightest, most dense shading represents a packed-bed state ($\epsilon \sim 0.4$), and black (no dots) represents all gas ($\epsilon = 1.0$). The right side of Figure 7 is a contour plot representation of the computed porosity distribution at the same time (0.255 s), with superimposed solids-phase velocity vectors. Comparing the dot and contour plot representations shows that the perceived edge of the bubble is a contour of porosity, ϵ, of about 0.8. Previous studies have shown that this choice is usually consistent with experimental bubble size and also with strong porosity gradients that exist at the bubble boundary (e.g., Gidaspow and Ettehadieh, 1983).

Figures 2b and 7 show generally good agreement. The predicted sizes shown in Table 2 and location of the first bubble agree well with the experimental results, and the expanded bed height and shape are approximately correct. The slight asymmetries present in the experiment were not accounted for in the model. Thus, the formation of a vortex street above the obstacle (which appears to sweep particles back and forth, keeping them from piling up) is absent, and the computations show a solids buildup.

A computation utilizing a finer mesh was performed to obtain better results. The same number of computational cells in the x-direction was used, but the number in the y-direction was increased to 48 ($\Delta y = 1.217$ cm). This change made the cell aspect ratio much closer to unity ($\Delta y/\Delta x = 1.92$) than was the case for the 31 × 12 node computational mesh ($\Delta y/\Delta x = 7.67$). In these computations, a fixed time step of 10^{-5} s was used. The result of these computations is shown in Figure 8 for times corresponding closely to those of Figure 2. The agreement between

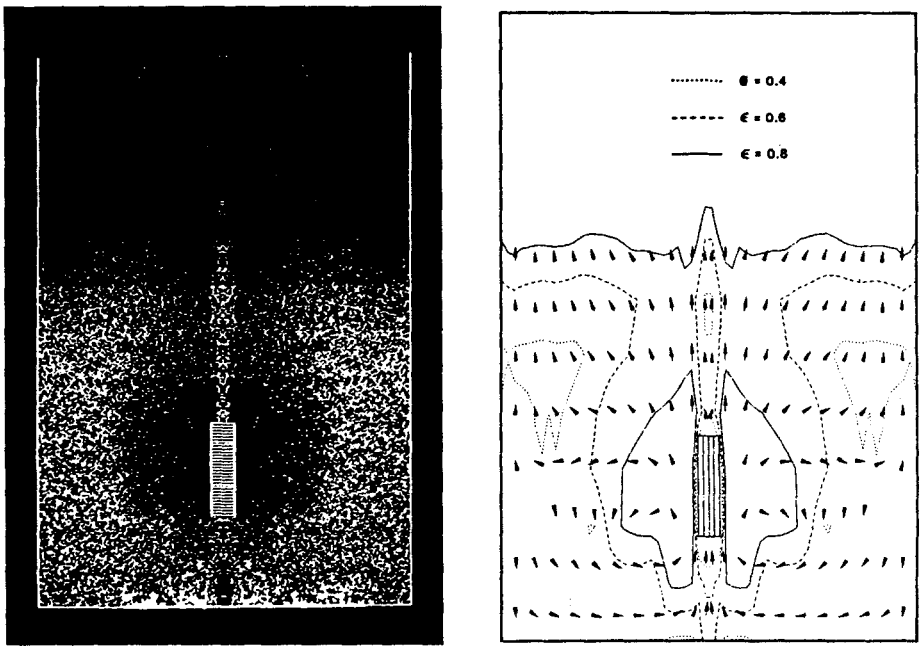

Figure 7. Computer-generated porosity distributions for a two-dimensional fluidized bed with an obstacle, at 0.255 s, 31 × 12 nodes.

Hydrodynamic Model A, solids elastic modulus G_1 (left, dot plot; right, contour plot)

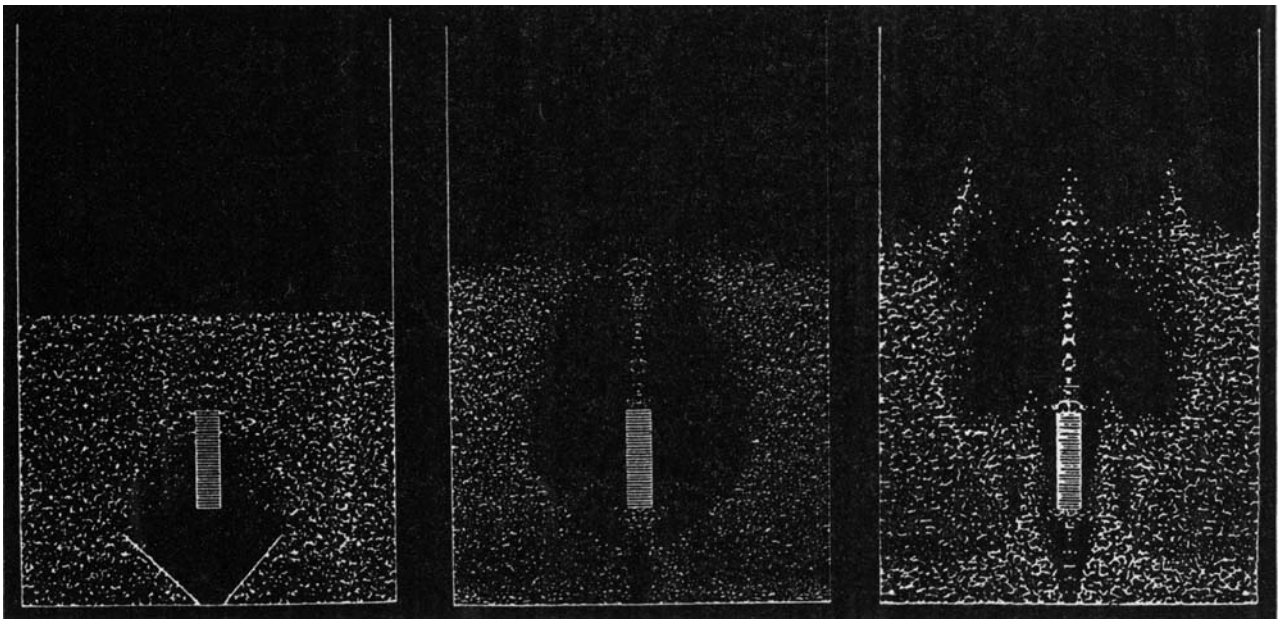

a b c

Figure 8. Computer-generated porosity distribution for a two-dimensional fluidized bed with an obstacle, 31 × 48 nodes.

Hydrodynamic Model A, solids elastic modulus G_1, (a. 0.13 s; b. 0.255 s; and c. 0.32 s)

the computations using the 31 × 12 node mesh and the 31 × 48 node mesh is good, as can be seen by comparing Figures 7 and 8b. The expanded bed shape is in better agreement with the experiment and is also sharper, indicating that the bed interface is resolved better with the finer mesh. Fine details, such as the splash of solids against the bottom of the obstacle, are also better resolved. The price paid for the finer resolution is considerably longer computing time (approximately 10 times longer than that using the coarser mesh).

The solids velocity and porosity patterns at 0.255 s plotted in Figure 7 indicate the existence of a vortex pattern in the wake of the rising bubble near the lower sides of the obstacle. Also revealed is a larger general solids-concentration pattern induced by the rising bubble. Such solids motions give rise to the erosion of immersed heat-exchanger tubes in fluidized-bed combustors.

With the 31 × 48 node mesh, it is possible to resolve the angularity of the bubble bottom. Figure 2a reproduces a still frame from the high-speed motion picture at about 0.11 s. At this time, the bed has barely expanded, and the size of the bubble is significantly less than at about 0.25 s as shown in Figure 2b. The bed height is just over 30.5 cm (12 in.). Figure 8a shows a dot plot representation of the computed porosity distributions at 0.13 s. Comparison of Figure 8a with Figure 2a reveals good agreement in terms of the bubble size and the angle at the bottom of the bubble. The experimental angle is 42°; the computed angle (solid line in Figure 8a), 36°, does not vary significantly over a ±0.02-s time span. The computed bed expansion is also in good agreement with experiment.

As shown in Figure 8, as time progresses beyond 0.25 s, the bubble splits, the bed height continues to expand, and particles are deflected away from the obstacle, causing a strong vortex pattern with solids moving down the walls. This computed sequence shown in Figure 8 compares well with the frames from the high-speed motion picture shown in Figure 2. After 1.5 s, the bed collapses to its initial height. The bed then begins to expand again, and the cycle repeats itself.

As was mentioned earlier, it was assumed for the computer simulation that the initial solids velocity is zero, that the bed porosity is uniform at 0.42, and that the gas mass flux corresponds to minimum-fluidization conditions. The high-speed motion picture study revealed that before the jet was turned on, very small bubbles originated from the side of the obstacle. This same phenomenon has been observed by other investigators (Buyevich et al., 1986; Glass and Harrison, 1964; Grace, 1982; Loew et al., 1979).

To predict the behavior of our fluidized bed at minimum fluidization, computations were performed with the central jet and the secondary air both at minimum fluidization, and with no assumption of symmetry. The number of nodes in the transverse direction was increased to 64 (from 33 for the coarse-mesh nodalization). The inlet velocity was maintained uniform at 26 cm/s. As can be seen in Figure 9, the incipient bubble formations are not quite symmetrical. This asymmetry is probably triggered by perturbations introduced into the uniform flow as a result of asymmetric sweeping through the computational cell during the iteration process. A bubble forms under the obstacle and moves upward, splitting in the process. The split bubbles then move up the sides of the obstacle and eventually out of the bed. More asymmetry resulted at later times, indicating an out of phase behavior was developing. Frame-by-frame examination of the computer-generated motion picture showed that bubbles formed below the obstacle and moved upward at a frequency of about 3 Hz. It is clear from Figure 9 that the fluidized bed was not in a completely uniform initial condition when the jet was

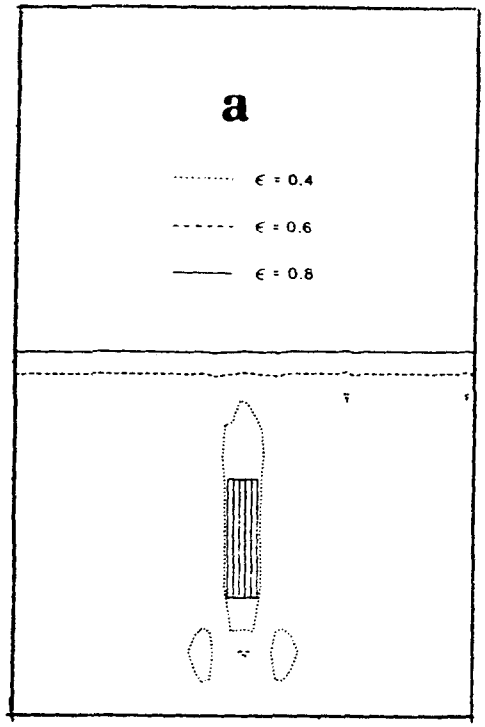

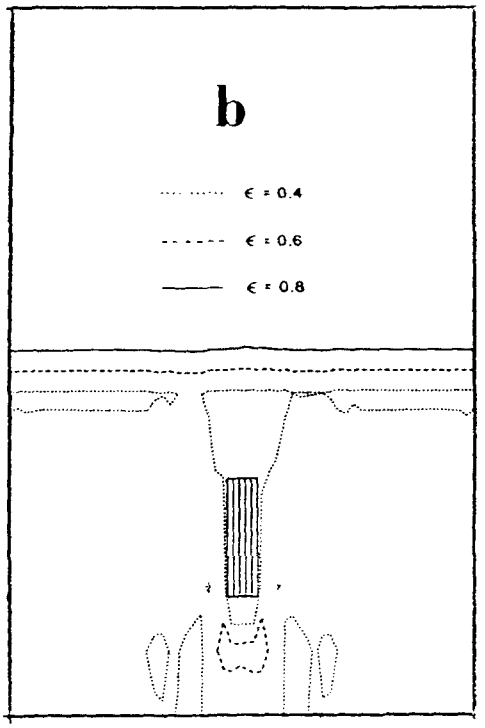

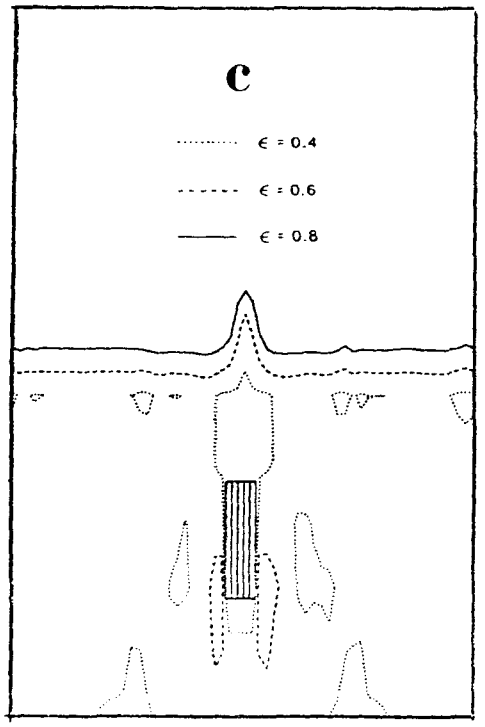

Figure 9. Computed porosity distribution in a two-dimensional fluidized bed at minimum fluidization with an obstacle.
(a. 0.1 s; b. 0.2 s; and c. 0.3 s)

turned on. This could explain some differences between the experiment and the calculated results. These differences should vanish for time-averaged results.

Parametric Study Using Two Hydrodynamic Models and Three Solids Elastic Moduli

A parametric study involving the solids elastic modulus, G, was conducted for Hydrodynamic Models A and B. To our knowledge, only one similar parametric study has been performed previously (Lee and Lyczkowski, 1981).

Bed dynamics

A comparison between experimental and computed bubbles at 0.255 s for the three solids elastic moduli, G_i, the coefficients of which have been discussed previously, was performed. It was found that the solids elastic modulus affects the instantaneous bed interface, bubble shape, and timing. A larger solids elastic modulus (G_2) gives rise to a larger solids stress, a somewhat larger bed expansion, and smaller bubbles. This occurs because the solids stress acts like a solids diffusion mechanism, as explained by Bouillard (1986). At minimum fluidization, the drag force exerted on the particles by the gas phase is balanced by the buoyancy force. The solids elastic modulus, G, although generally small, can alter this delicate balance and prevent bubbling by means of a dispersive mechanism (Bouillard, 1986).

The passage frequency of bubbles around the obstacle was computed to be about 4–5 Hz, which is somewhat higher than that without an obstacle (3–4 Hz) as shown in Figure 3 taken from Seo (1985). This increase in frequency is probably due to the lower drag resistance caused by the presence of the obstacle, which by diminishing the gas residence time increases the bubbling frequency. The predicted size and location of the first bubble, as well as the expanded bed height, agree well with experiments as shown in Table 2. No significant differences in bubble shapes, sizes, or bubbling frequencies between Hydrodynamic Models A and B were observed.

Detailed comparative and repeated frame-by-frame analysis of a computer-generated motion picture of the contour plot representation of the computed porosity distribution and the high-speed motion picture study revealed good agreement for the frequency (4–5 Hz) of bubbles around the obstacle (discussed above) and the higher frequency (9–10 Hz) of the small bubbles that form under the obstacle. These smaller bubbles can be seen under the obstacle in Figures 2, 4, 7, and 8. Glicksman and Lord (1980) reported similar oscillatory behavior of the dense phase around tubes immersed in fluidized beds.

As bubbles detach from the distributor, rise through the bed, and burst at the top of the bed, a solids-circulation pattern forms after the passage of the first bubble. Such a circulation is predicted equally well with Hydrodynamic Models A and B, and is shown in Figure 10, where solids velocity vectors are time-averaged over a period of 2 s. Two symmetric vortices in the lower part of the bed are computed, indicating strong solids circulations. These important solids motions explain why fluidized beds have excellent heat and mass transfers and why erosion takes place.

Transient porosities, pressures, and axial and lateral gas and solids velocities were computed using three sets of solids-elastic-modulus coefficients and the two hydrodynamic models (Bouillard, 1986). Typical results for the porosity fluctuations are shown in Figure 11 for solids elastic modulus G_1 and Hydrodynamic Models A and B. Other computed results are very similar and are not reported here.

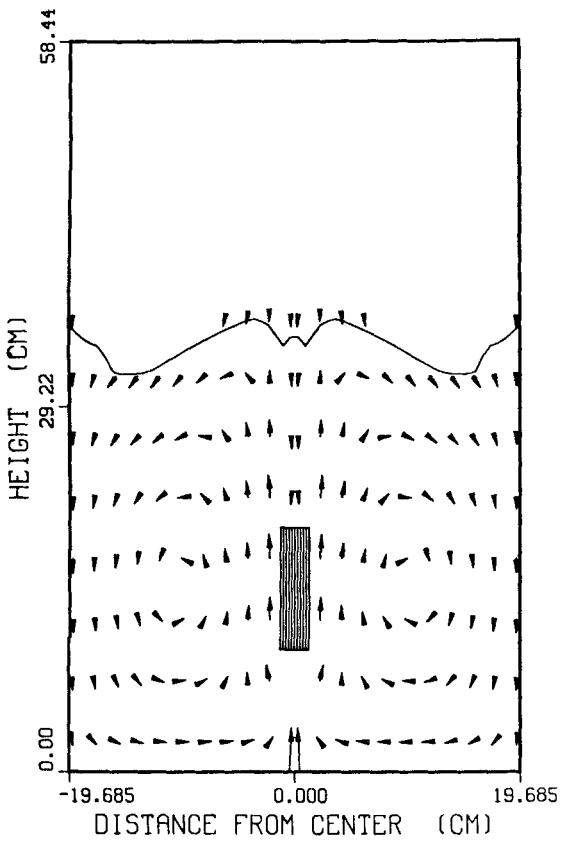

Figure 10. Predicted solids velocity field time-averaged over 2 s.

Computed with solids elastic modulus G_1, 31 × 12 nodes, for Hydrodynamic Model B

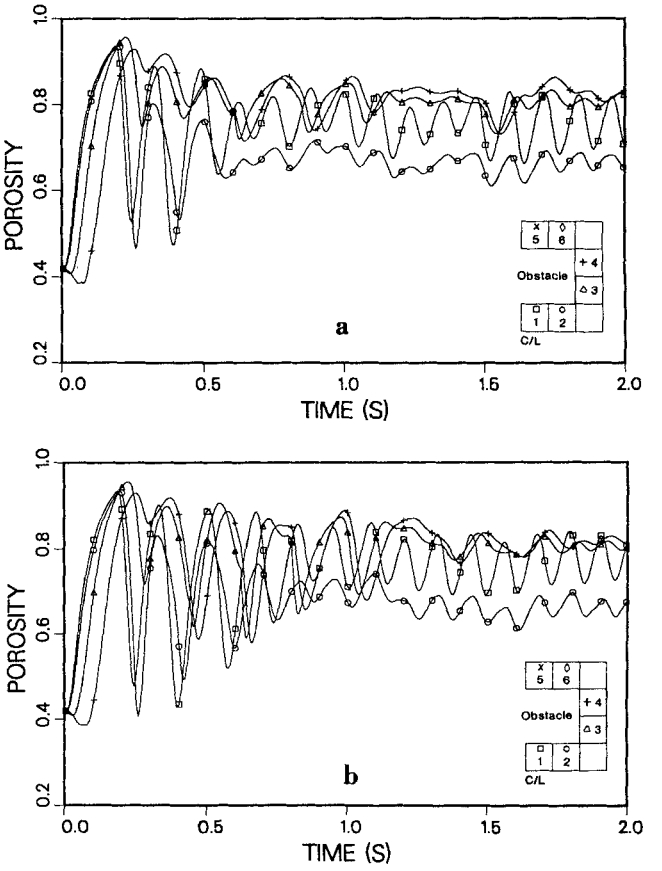

a. Hydrodynamic Model A
b. Hydrodynamic Model B

Figure 11. Computed transient porosity at four locations around obstacle, solids elastic modulus G_1.

Analysis of the computations clearly shows that under the obstacle (locations 1 and 2), computed porosities, gas and solids velocities, and pressures oscillate at a frequency of approximately 10 Hz, which is in excellent agreement with the observed frequencies determined from the frame-by-frame analysis of the high-speed motion pictures of the experiment. With Hydrodynamic Model B, somewhat greater amplitudes appear in these variables at start-up (between 0 and 0.8 s). Afterward, oscillatory behaviors of the bed predicted from these two models are almost identical. Pressure and porosity oscillations are in phase, while axial gas and solids velocity oscillations are in phase with each other but out of phase (by almost a full 90°) with pressure oscillations, as should be expected. On the side of the obstacle (locations 3 and 4), computed results oscillate at a frequency of 4–5 Hz, which is also in excellent agreement with the bubble frequency determined from the frame-by-frame analysis of the high-speed motion pictures of the experiment.

The effect of the solids elastic moduli G_1 and G_3, was studied for Hydrodynamic Model A (Bouillard, 1986). The frequency of approximately 10 Hz under the obstacle (positions 1 and 2) was found to be nearly independent of this parameter. In the defluidized region, solids elastic modulus G_3 gives unrealistically low porosities (as low as $\epsilon = 0.3$). Elsewhere, G_3 yielded porosities below 0.2. Therefore, the Rietema and Mutsers (1973) model used previously (Ettehadieh et al., 1984; Gidaspow et al., 1981, 1982, 1983a,b; Gidaspow, 1986; Gidaspow and Etteha-

dieh, 1983) is judged to be inadequate for cases involving obstacles.

The conclusion reached from this parametric study is that the computed bubbles do vary slightly, but all are in generally good agreement with those observed in the high-speed motion picture study. This agreement suggests that the solids flow patterns are also reasonably correct, although they have not yet been measured. Multiple experimental runs should be performed so that the slightly different bubble patterns that result from random variations in initial conditions from run to run can be averaged out.

Time-averaged porosity distributions

Computed time-averaged porosity distributions using Hydrodynamic Models A and B are shown in Figure 12. These distributions were computed with solids elastic modulus G_1. Computed time-averaged void fractions were obtained by averaging the calculated porosity from 1.5 to 2.0 s in order to eliminate the influences of the start-up and to ensure a well-established oscillatory behavior of the bed. Error bars represent the range of computed deviations from the time-averaged profiles obtained over different time intervals. The experimental and theoretical time-averaged porosity distributions are very similar (compare Figures 4 and 12) but some differences do occur. These are felt to be principally due to asymmetries present in the experiment and simplified solids rheology. Away from the jet and near the walls, porosities tend to be constant at $\epsilon \sim 0.4$, which represents the minimum-fluidization porosity. Characteristic ellipsoidal profiles are found below the obstacle and in the dilute region near the jet mouth. In the lower part of the bed, near the distributor, the solids tend to pack and form a slumped or "dead" region. In this region, the two predictions seem to differ, and Hydrodynamic Model B seems to predict more realistic porosity contours.

A possible explanation can be suggested by comparing Eq. 4 with Eq. 10, and Eq. 6 with Eq. 12. Unlike hydrodynamic model A, hydrodynamic model B does not have a pressure term in the solids phase momentum equations. Thus, the solids would be expected to compact more with Hydrodynamic Model B.

Another difference between theory and experiment is the shape of the time-averaged expanded bed height. In our calculations, the isoporosity contour $\epsilon = 0.80$ curves upward at the wall; in the experiments, however, it flattens horizontally. We speculate that this discrepancy is due to the lower accuracy in the porosity measurements at the wall (Bouillard, 1986). Moreover, contouring is very sensitive to the prescribed porosity. Another reason for the differences may be the neglect of the solids viscous stresses which reflects simplifications made in the solids rheology. The differences in the positions of the isoporosity contour of $\epsilon = 0.7$ are due primarily to asymmetries present in the experiment.

Theoretical and experimental vertical time-averaged porosity

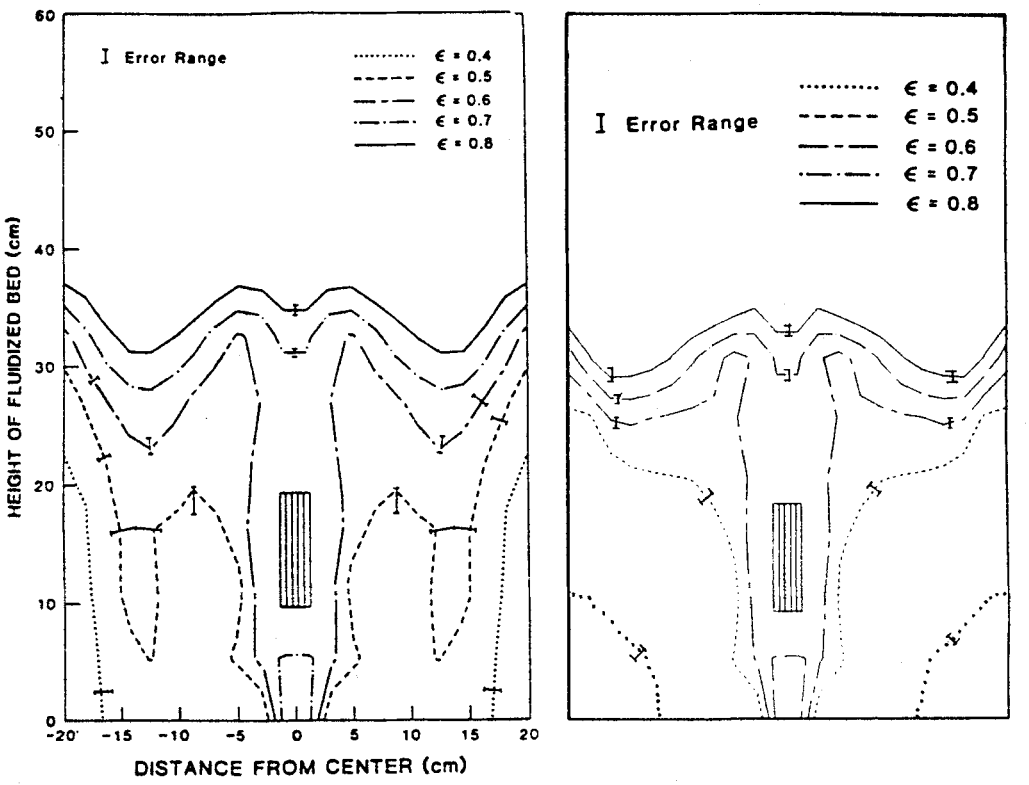

Figure 12. Predicted time-averaged porosity distributions computed with the solids elastic modulus G_1.

a. Hydrodynamic Model A
b. Hydrodynamic Model B

profiles were compared at 2.5, 10, and 17 cm from the center of the bed as shown in Figure 13. These three zones represent the center region, highly influenced by the jet (2.5 cm); the middle region (10 cm), partially influenced by the jet; and the slumped region (17 cm), not influenced by the jet. Time-averaged predictions from the two models are almost identical. At 2.5 cm from the center of the bed, a maximum-porosity region (ϵ = 0.65–0.70) exists between 8 and 16 cm from the distributor. This region, which corresponds to a time-averaged gas layer that exists because of the passage of bubbles, is predicted with all three solids elastic moduli, G_1, G_2, and G_3. There is a discrepancy between predicted and experimental porosities in the defluidized region above the obstacle due to asymmetries present in the experiment that are not taken into account in these calculations.

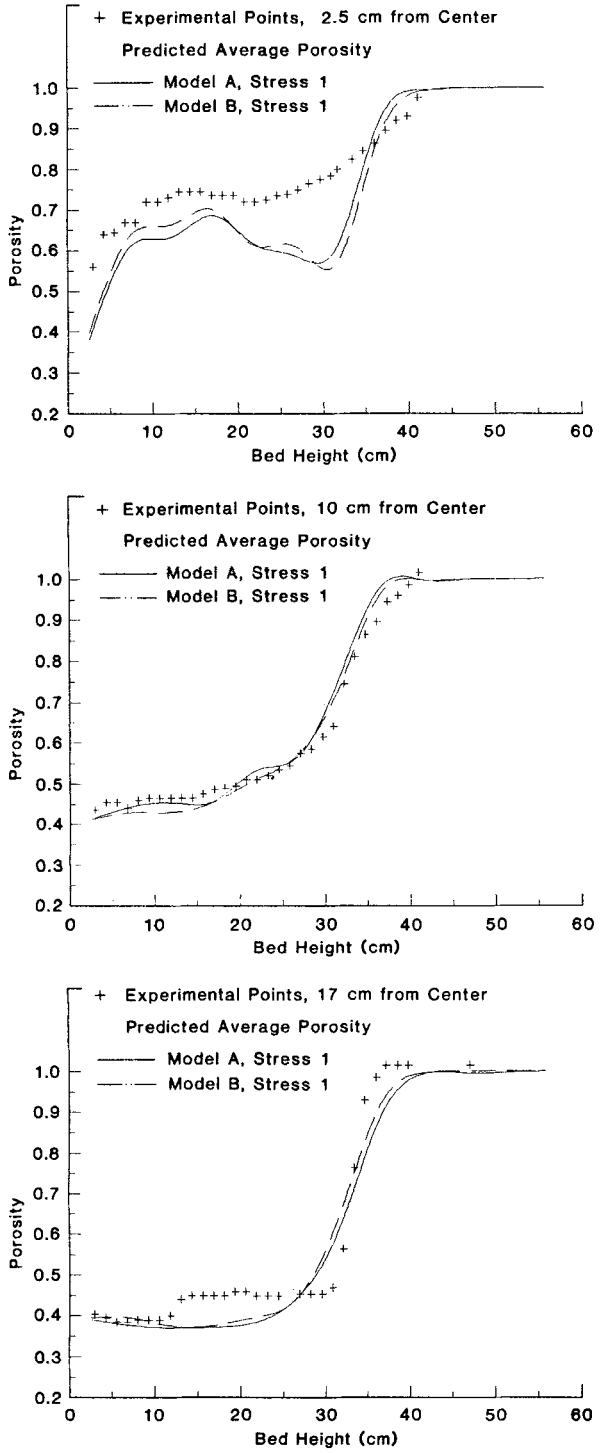

Figure 13. Experimental and theoretical vertical time-averaged porosity profiles for two hydrodynamic models, solids elastic modulus G_1.

Vertical time-averaged porosity profiles at 17 cm from the center showed the same effect of the solids elastic modulus (Bouillard, 1986). In the regions of high solids volume fractions, the solids elastic modulus, G_3, of Rietema and Mutsers (1973) predicts unrealistically low porosities ($\epsilon \sim 0.3$), especially in the slumped region. As Figure 5 shows, at low porosities ($\epsilon \sim 0.4$) this elastic modulus is indeed too small to predict correctly the dense phase behavior. On the other hand, solids elastic moduli G_1 and G_2 give good predictions of the behavior of the slumped regions, because their value becomes important at $\epsilon = \epsilon^* = 0.378$ or $\epsilon = \epsilon^* = 0.41$ (see Figure 5).

Conclusions

Bubbling and solids motion in a fluidized bed with an immersed obstacle were predicted using two hydrodynamic models without the use of fitted parameters. The first model includes a pressure drop in the solids phase; the second model has this pressure drop set to zero.

Computed porosities around the immersed obstacle were found to oscillate at 4–5 Hz, those below the obstacle at 9–10 Hz. These computed frequencies are in good agreement with those obtained from repeated frame-by-frame analysis of a high-speed motion picture study taken of a thin "two-dimensional" rectangular fluidized bed containing a rectangular obstacle above a central jet located in the middle of the gas distributor. Surprisingly, time-averaged porosity distribution computed with both these two hydrodynamic models agree with those measured with a gamma-ray densitometer. The only major source of disagreement is at the top of the obstacle due to asymmetries present in the experiment. No major differences between the two hydrodynamic models were observed.

A parametric study varying the value of the solids elastic modulus showed that the computed amplitudes and time-averaged values of transient porosities and gas and solids velocities are affected to some extent but all are in generally close agreement.

Acknowledgments

This work was performed for the U.S. Department of Energy, Morgantown Energy Technology Center. The Project Manager for the first year (Oct. 1, 1984, through Sept. 30, 1985) was Thomas J. O'Brien. We thank him for his many suggestions and helpful comments, and particularly for his moral and financial support. We also wish to thank Holmes A. Webb, who has managed the project since October 1, 1985, for his numerous suggestions and continued support.

We thank Shyh-Tsung Cheng for measuring the experimental time-averaged porosities, Yong-Chil Seo for taking the high-speed motion pictures, and the National Science Foundation for financial support for the experimental phase of this work.

Notation

C = characteristic direction, m/s
C_d = drag coefficient (Eq. 23)
c = compaction modulus
d_p = particle diameter, m

G = solids elastic modulus, Pa
g = acceleration due to gravity, m/s^2
P = pressure, Pa
Re_y = Reynolds number of solid particle (Eq. 24)
t = time, s
U_g, U_s = gas- and solids-phase velocities, respectively, in the x-direction, m/s
V_g, V_s = gas- and solids-phase velocities, respectively, in the y-direction, m/s
x = lateral coordinate, m
y = axial coordinate, m

Greek letters

β_x, β_y = fluid-particle friction coefficient in the x- and y-directions, respectively, kg/(m^3 · s)
ϵ = gas-phase volume fraction (porosity)
ϵ_g = void fraction = ϵ
ϵ_{mf} = gas volume fraction at minimum fluidization
ϵ_s = solids-phase volume fraction = $1 - \epsilon$
ϵ^* = compaction gas-phase volume fraction
τ = solids stress, related to particle-to-particle pressure, Pa
μ_g = gas viscosity, Pa · s
ρ_s, ρ_g = solids- and gas-phase densities, respectively, kg/m^3
ϕ_s = sphericity of particles (shape factor); $0 < \phi_s \leq 1$

Literature Cited

Altiner, H. K., and J. F. Davidson, "Power Flow from an Aerated Hopper," *Fluidization,* J. R. Grace and J. M. Madsen, eds., Plenum Press, New York, 461 (1980).

Bird, R. B., W. E. Stewart, and E. N. Lightfoot, *Transport Phenomena,* 3rd Printing, Wiley, New York (1960).

Bouillard, J. X., "Hydrodynamics of Sedimentation, Fluidization, and Erosion," PhD Diss., Illinois Institute of Technology, Chicago (Dec., 1986).

Buyevich, Y. A., V. N. Korolyov, and N. I. Syromyatnikov, "Hydrodynamic Conditions for the External Heat Exchange in Granular Beds," *Heat and Mass Transfer in Fixed and Fluidized Beds,* W. P. M. van Swaaij and N. H. Afghan, eds., 333, Hemisphere, Washington, DC (1986).

Concha, F., and M. C. Bustos, "A Modification of the Kynch Theory of Sedimentation," *AIChE J.,* **33,** 312 (1987).

Ergun, S., "Fluid Flow through Packed Columns," *Chem. Eng. Prog.,* **48**(2), 89 (1952).

Ettehadieh, B., D. Gidaspow, and R. W. Lyczkowski, "Hydrodynamics of Fluidization in a Semicircular Bed with a Jet," *AIChE J.,* **30**(4), 529 (1984).

Fakhimi, S., and D. Harrison, "The Void Fraction near a Horizontal Tube Immersed in a Fluidized Bed," *Trans. Inst. of Chem. Engs.,* **58,** 125 (1980).

Fanucci, J. B., N. Ness, and R. H. Yen, "On the Formation of Bubbles in Gas-Particulate Fluidized Beds," *J. Fluid Mech.,* **94**(2), 353 (1979).

Garg, S. K., and J. W. Pritchett, "Dynamics of Gas-Fluidized Beds," *J. Appl. Phys.,* **46,** 4493 (1975).

Gidaspow, D., "Hydrodynamics of Fluidization and Heat Transfer: Supercomputer Modeling," Heat Transfer Conf., Denver (Aug. 5, *1985); Appl. Mech. Rev.,* **39**(1), 1 (Jan., 1986).

Gidaspow, D., and B. Ettehadieh, "Fluidization in Two-Dimensional Beds with a Jet: 2. Hydrodynamic Modeling," *Ind. and Eng. Chemist. Fund.,* **22,** 193 (1983).

Gidaspow, D., B. Ettehadieh, and R. W. Lyczkowski, "Computer Modeling of Fluidization of Sand in a Two-Dimensional Bed with a Jet," AIChE Meeting (Nov. 8–12, 1981).

Gidaspow, D., B. Ettehadieh, C. Lin and R. W. Lyczkowski, "Theoretical and Experimental Hydrodynamics of a Jet in a Fluidized Bed of Particles," *Proc. Int. Symp. on Powder Technol.,* K. Iinoya, K. Beddow, and G. Jimbo, eds., 672, Society of Powder Technology, Kyoto, Japan (1982).

Gidaspow, D., C. L. Lin, and Y. C. Seo, "Fluidization in Two-Dimensional Beds with a Jet: 1. Experimental Porosity Distribution," *Ind. and Eng. Chemist. Fund.,* **22,** 187 (1983a).

Gidaspow, D., Y. C. Seo, and B. Ettehadieh, "Hydrodynamics of Fluidization: Experimental and Theoretical Bubble Sizes in a Two-Dimensional Bed with a Jet," *Chem. Eng. Commun.,* **22,** 253 (1983b).

Gidaspow, D., and M. Syamlal, "Solid-Gas Critical Flow," AIChE Meeting, Chicago (Nov. 10–15, 1985).

Glass, D. H., and D. Harrison, "Flow Patterns near a Solid Obstacle in a Fluidized Bed," *Chem. Eng. Sci.,* **19,** 1001 (1964).

Glicksman, L. R., and W. K. Lord, "Predictions of Bubble Growth in Bubble Chains," *Fluidization,* J. R. Grace and J. M. Madsen, eds., Plenum Press, New York, 125 (1980).

Grace, J. R., "Fluidized-Bed Hydrodynamics," *Handbook of Multiphase Systems,* G. Hetsoroni, ed., Ch. 8.1, McGraw-Hill, New York (1982).

Harlow, F. H., and A. A. Amsden, "Numerical Calculation of Multiphase Fluid Flow," *J. Comp. Phys.,* **17,** 19 (1975).

Jackson, R., "Hydrodynamic Stability of Fluid-Particle Systems," *Fluidization,* 2nd ed., J. F. Davidson, R. Clift, and D. Harrison, eds. 47, Academic Press (1985).

Jackson, R., "The Mechanics of Fluidized Beds," *Trans. Inst. of Chem. Engrs.,* **41,** 13 (1963).

Kunii, D., and O. Levenspiel, *Fluidization Engineering,* Wiley, New York (1969).

Lee, W. H., and R. W. Lyczkowski, "The Basic Character of Five Two-Phase Flow Model Equation Sets," *Proc. Int. Topical Meeting on Advances in Mathematical Methods for the Solution of Nuclear Engineering Problems,* **1,** 489, Amer. Nucl. Soc., La Grange Park, IL (1981).

Levy, E. K., R. A. Freeman, and S. Caram, "Effect of Horizontal Tubes on Bubble Eruption Behavior in Gas Fluidized Beds," *Proc. Engineering Foundation Conf. on Fluidization,* K. Ostergaard and A. Sorensen, eds., 135, Elsinore, Denmark (1986).

Levy, E. K., H. S. Caram, J. C. Dille, and S. Edelstein, "Mechanisms for Solids Ejection from Gas-Fluidized Beds," *AIChE J.,* **29**(3), 383 (1983).

Loew, O., B. Schmutter, and W. Resnick, "Particle and Bubble Behavior and Velocities in a Large-Particle Fluidized Bed with Immersed Obstacles," *Powder Technol.,* **22,** 45 (1979).

Lyczkowski, R. W., "Transient Propagation Behavior of Two-Phase Flow Equations," *Heat Transfer: Research and Application,* J. C. Chen, ed., *AIChE Symp. Ser.,* **75**(174):165–174, American Institute of Chemical Engineers, New York (1978).

Lyczkowski, R. W., D. Gidaspow, and C. W. Solbrig, "Multiphase Flow Models for Nuclear, Fossil, and Biomass Energy Production," *Advances in Transport Processes,* **2,** 198, A. S. Mujumdar and R. A. Mashelkar, eds., Wiley, New Delhi, India (1982).

Lyczkowski, R. W., D. Gidaspow, C. W. Solbrig, and E. D. Hughes, "Characteristics and Stability Analyses of Transient One-Dimensional Two-Phase Flow Equations and Their Finite Difference Approximations," *Nucl. Sci. and Eng.,* **66,** 378 (1978).

Mao, Q. M., and O. E. Potter, "Fluid-Bed Reactions with Horizontal Tubes as Internals," *Proc. Engineering Foundation Conf. on Fluidization,* K. Ostergaard and A. Sorensen, eds., 449, Elsinore, Denmark (1986).

Molerus, O., "Theory of Yield of Cohesive Powders," *J. Powder Technol.,* **12,** 259 (1975).

Nakamura, K., and C. E. Capes, "Vertical Pneumatic Conveying: A Theoretical Study of Uniform and Annular Particle Flow Models," *Can. J. Chem. Eng.,* **51,** 39 (1973).

NCB (IEA Grimethorpe) Ltd., *Overall Project Review,* Grimethorpe, Barnsley, U.K. (May, 1985).

Orr, Jr., C., *Particulate Technology,* Macmillan, New York, 421 (1966).

Padhye, A., and T. O'Brien, "Computer Simulation of Cold Flow Studies of the Westinghouse Gasifier," Energy Source Technology Conf. Exhibition, preprint (1984).

Pemberton, S. T., and J. F. Davidson, "Elutriation from Fluidized Beds: I. Particle Ejection from the Dense Phase into the Freeboard," *Chem. Eng. Sci.,* **41**(2), 243 (1986).

Piepers, H. W., E. J. E. Cottar, A. H. M. Verkooijen and K. Rietema, "Effects of Pressure and Type of Gas on Particle-Particle Interaction and the Consequences for Gas-Solid Fluidization Behavior," *J. Powder Technol.,* **37,** 55 (1984).

Pritchett, J. W., H. B. Levine, T. R. Blake and S. K. Garg, "A Numerical Model of Gas Fluidized Beds," *AIChE Symp. Ser.,* **74**(176), 134 (1978).

Prosperetti, A., "Numerical Aspects of the Simmer-II Code," *Multiphase Processes in LMFBR Safety Analysis*, A. V. Jones, ed., 197, Harwood Academic Publishers, Paris (1984).
Rietema, K., and S. M. P. Mutsers, "The Effect of Interparticle Forces on Expansion of a Homogeneous Gas-Fluidization," *Proc. Int. Symp. on Fluidization*, Toulouse, France, 32 (1973).
Rivard, W. C., and M. D. Torrey, "K-FIX: A Computer Program for Transient, Two-Dimensional, Two-Fluid Flow," Los Alamos Scientific Laboratory Report LA-NUREG-6623 (Apr., 1977).
Rivard, W. C., and M. D. Torrey, "K-FIX: A Computer Program for Transient Two-Fluid Flow—THREED: An Extension of the K-FIX Code for Three-Dimensional Calculations," Los Alamos Scientific Laboratory Report LA-NUREG-6623, Suppl. II (Jan., 1979).
Rowe, P. N., and D. J. Everett, "Fluidized Bed Bubble Viewed by X-Rays: Part I. Experimental Details and the Interaction of Bubbles with Solid Surfaces," *Trans. Instn. Chem. Engrs.*, **50**, 42 (1972).
Rowe, P. N., and H. Masson, "Interaction of Bubbles with Probes in Gas Fluidized Beds," *Trans. Inst. Chem. Engrs.*, **59**, 176 (1981).
Rudinger, G., and A. Chang, "Analysis of Non-Steady Two-Phase Flow," *Physics of Fluids*, **7**, 1747 (1964).
Seo, Y. C., "Fluidization of Single and Binary Size Particles," PhD Diss., Illinois Institute of Technology, Chicago (1985).
Shinohara, K., "Rheological Property of Particulate Solids," *Handbook of Powder Science and Technology*, M. E. Fayed and L. Otten, eds., Van Nostrand Reinhold, New York, 129 (1984).
Soo, S. L., *Fluid Dynamics of Multiphase Systems*, Blaisdell Publishing Co., Waltham, MA (1967).
Stewart, H. B., "Stability of Two-Phase Flow Calculations Using Two-Fluid Models," *J. Comp. Phys.*, **33**, 259 (1979).
Travis, J. R., F. H. Harlow, and A. A. Amsden, "Numerical Calculation of Two-Phase Flows," *Nucl. Sci. and Eng.*, **61**, 1 (1976).
Wen, C. Y., and Y. H. Yu, "Mechanics of Fluidization," B. S. Lee, ed., *AIChE Symp. Ser.*, **62**(62), 100 (1966).
Xavier, A. M., D. A. Lewis, and J. F. Davidson, "The Expansion of Bubbling Fluidized Beds," *Trans. Instn. of Chem. Engrs.*, **56**, 274 (1978).

Manuscript received Aug. 4, 1987, and revision received Mar. 6, 1989.